Supplemental Appendix

Methods:

Protein purification and labeling.

Myosin: Skeletal myosin (rabbit) was purified as described by Margossian et al., (1) and stored at -20ºC in 10 mM Tris, 600 mM KCl with 50 % glycerol. Prior to digestion with chymotrypsin, the frozen myosin was dialyzed into 20 mM Tris pH 7.0, 30 mM KCl, centrifuged to sediment the resulting myosin filaments and then dissolved in 20 mM Tris pH 7.0, 0.6M KCl, 2 mM $MgCl_2$. We then digested the dissolved myosin with α-chymotrypsin (*Sigma-Aldrich*, 0.025 mg/ml final concentration) for 10 minutes at 25ºC followed by addition of pefabloc (*Roche*, 5 mM final concentration) and then dialyzed the reaction into either 20 mM Tris pH 7.0, 30 mM KCl, and 2 mM $MgCl_2$, for storage on ice prior to experiments or into 20 mM Tris pH 7.0, 30 mM KCl, and 2 mM $MgCl_2$ followed by desalting into 10 mM Tris pH 7.0 with 150 mM Sucrose prior to snap freezing in liquid nitrogen for storage at -80ºC.

RLC: The chicken gizzard smooth muscle myosin regulatory light chain with a single reactive cysteine at position 108 was expressed in *E. coli*. as described in our previous work (2) and purified by inclusion body isolation followed by ion exchange chromatography (2). We labeled the purified cgRLC with 5 molar excess of Alexa-488 (*Invitrogen*) overnight at 4º C and then removed free dye by gel filtration chromatography. The labeled RLC was snap frozen in liquid nitrogen and stored at -80ºC. Labeling efficiency was 100% determined by the molar extinction coefficient of the Alexa dye and the measured RLC protein concentration, determined by the Bradford assay using a BSA standard.

Actin: Actin was purified from rabbit skeletal muscle by acetone dehydration followed by extraction into ice cold water as described in our previous work (3) and then polymerized in 10 mM Tris pH 7.5, 3 mM $MgCl_2$, 0.5 mM ATP and stored on ice prior to use. For phosphate release experiments, the F-actin was stabilized with stochiometric excess of phalloidin (*Sigma Aldrich*), followed by 24 h dialysis (3 buffer changes) into 10 mM Tris pH 7.0 with 2 mM $MgCl_2$.

Protein and dye concentration: The Bradford protein concentration assay utilizing a known BSA protein standard was used throughout this study to determine protein concentrations. Reagents for this assay were purchased from *Biorad*. The extinction coefficient for the Alexa-488 dye is 73,000 at 495 nm, and for Cy3 is 136,000 at 570 nm, per manufacturers specifications.

Exchange: We exchange the Alexa labeled RLC onto HMM by combining the two proteins (3 molar excess RLC to HMM) in 50 mM Tris pH 7.5, 120 mM KCl, 2 mM DTT, 12 mM EDTA (4) and then incubated the reaction mix for 30 minutes at 30ºC. After the incubation, we adjusted the reaction to 12 mM $MgCl_2$ and then incubated the mixture on ice for 15 minutes followed by dialysis into 10 mM Tris pH 7.0, 30 mM KCl, 2 mM $MgCl_2$ prior to gel filtration to remove free RLC.

Buffers and solutions: All experiments, unless otherwise noted, were performed in 10 mM Tris pH 7.0, 2 mM $MgCl_2$ at 25ºC.

Steady-state ATPase activity. We measured actin-activated MgATPase activity using an NADH-coupled assay (5) performed at 25ºC in 10 mM Tris pH 7.0, 2 mM $MgCl_2$. The reaction mix contained varied [actin], and 0.2 mM NADH, 0.5 mM PEP, 2.1 mM ATP, 10 U/mL LDH, 40 U/mL PK, HMM 50-100 nM HMM. We acquired absorbance at 340 nm every 10 seconds for 120 seconds total using a Beckman-Coulter DU640B spectrophotometer.

Transient kinetics. Transient biochemical experiments with steady-state fluorescence (total fluorescence intensity) detection were performed on an *Applied Photophysics* stopped-flow spectrophotometer capable of sequential mixing experiments. The single-mix dead time for this instrument is 1.3 ms, calibrated using fluorescence enhancement of 8-hydroxyquinoline following Mg^{+2} binding under pseudo first-order kinetics conditions (6). All buffers were filtered and then degassed for 30 minutes under high-vacuum prior to use. All

stopped-flow experiments were performed at 25°C maintained by a circulating water bath. Transient time-resolved FRET (millisecond-resolved transient biochemical experiments with nanosecond-resolved fluorescence detection), $(TR)^2$FRET, was measured using a transient time-resolved fluorescence spectrophotometer (7-9). This instrument utilizes a *Biologic USA* SFM/20 single-mix stopped-flow accessory coupled to our transient time-resolved fluorescence spectrophotometer. The dead time for the instrument was 1.8 ms, calibrated using the 8-hydroxyquinoline + Mg^{+2} control reaction (6). For experiments mixing equilibrated myosin in the presence of 10 molar excess ATP with actin containing 1 mM MgATP, we loaded the actin into syringe A, followed by a freshly prepared 600 μL mixture of myosin + Cy3-ATP in syringe B and then immediately mixed with the actin in syringe A.

$(TR)^2$FRET: The TRF and $(TR)^2$F spectrometers, originally described in our previous work (7-9), transiently digitize the time-resolved fluorescence emission following a 1 ns laser pulse. The laser used in this study is an artisanal 473 nm microchip laser (FP2-473-3-5) with an LD-702 controller hand crafted by *Concepts Research Corporation*, in WI, operating at 5 KHz repetition frequency. Thus samples are excited every 0.2 ms. For equilibrium and steady-state biochemical conditions, 1000 replicate waveforms were signal-averaged prior to analysis. For transient time-resolved measurements acquired after rapid mixing by stopped-flow, 5 waveforms were averaged every 1 ms. Total time-resolved fluorescence was measured with the emission polarizer set to the magic angle (54.7°) or removed. For polarized time-resolved fluorescence measurements (TR-F Anisotropy), the emission polarizer was set successively to 0°, 54.7°, and 90°.

$(TR)^2$FRET Data Analysis

Total fluorescence: We determined the total fluorescence emission for FRET samples by integrating the $(TR)^2$FRET waveforms over the nanosecond decay time after subtracting the pre-trigger dark current, ~5% in amplitude compared to the maximum waveform intensity.

TR-FRET: TRF waveforms from donor and FRET-labeled samples were analyzed as described in our previous publications (7-9) Eq. 1-13, paraphrased below. The measured time-resolved fluorescence waveform, $I(t)$ (Eq 1),

$$I(t) = \int_{-\infty}^{\infty} \mathrm{IRF}(t - t') \cdot F(t') dt' \qquad \text{Eq. 1}$$

is a function of the nanosecond decay time, t, and is modeled as the convolution integral of the measured instrument response function, IRF(t), and the fluorescence decay model, $F(t)$. The fluorescence decay model (Eq. 2)

$$F(t) = x_D F_D(t) + (1 - x_D)\, F_{DA}(t) \qquad \text{Eq. 2}$$

is a linear combination of a donor-only fluorescence decay function, $F_D(t)$ and an energy transfer-affected donor fluorescence decay, $F_{DA}(t)$. The donor decay $F_D(t)$ is a sum of exponentials (Eq. 3)

$$F_D(t) = \sum_{i=1}^{2} A_i \, exp(-t/\tau_i) \qquad \text{Eq. 3}$$

with discrete lifetime species τ_i and pre-exponential mole fractions A_i. For the Alexa-488 donor two exponentials were required to fit the observed fluorescence. The energy transfer-affected donor decay function, $F_{DA}(t)$ (Eq. 4),

$$F_{DA}(t) = \sum_{j=1}^{2} X_j \cdot T_j(t) \qquad \text{Eq. 4}$$

is a sum over multiple structural states (j) with mole fractions X_j, represented by FRET-affected donor fluorescence decays $T_j(t)$. The increase in the donor decay rate (inverse donor lifetime) due to FRET is given by the Förster equation

$$k_{Ti} = k_{Di}(R/R_{0i})^{-6}, \text{ where} \qquad \text{Eq. 5}$$

$$k_{\mathrm{DAi}} = k_{\mathrm{Di}} + k_{\mathrm{Ti}}, \text{and} \quad \text{Eq. 6}$$

$$k_{\mathrm{Di}} = 1/\tau_{\mathrm{i}} \quad \text{Eq. 7}$$

We modeled TR-FRET assuming that each structural state *j* (Eq. 4) corresponds to a Gaussian distribution of interprobe distances, $\rho_j(R)$:

$$T_{\mathrm{j}}(t) = \int_{-\infty}^{\infty} \rho_{\mathrm{j}}(R) \cdot \sum_{i=1}^{3} A_{\mathrm{i}}\, exp\left(\frac{-t}{\tau_{\mathrm{i}}} \cdot \left[1 + \left(\frac{R_{0\mathrm{i}}}{R}\right)^6\right]\right) dR \quad \text{Eq. 8}$$

$$\rho_{\mathrm{j}}(R) = \frac{1}{\sigma_{\mathrm{j}}\sqrt{2\pi}} \exp\left(\frac{-\left[R - R_{\mathrm{j}}\right]^2}{2\sigma_{\mathrm{j}}^2}\right) \quad \text{Eq. 9}$$

$$\sigma_{\mathrm{j}} = \mathrm{FWHM_j}/\left(2\sqrt{2\ln 2}\right) \quad \text{Eq. 10}$$

As with our previous work (7-9) , R_{0i} is calculated according to Eq. 11 from the spectral overlap integral, *J*, the orientation-sensitive term κ^2, the refractive index n, and the donor quantum yield Q_{Di} (Eq. 12-14). $\langle Q_D \rangle$ was measured as 0.91 ± 0.01, by comparison to a quinine sulfate fluorescence standard in 50 mM H_2SO_4 at 25°C according to Eq. 14 (1, 4).

$$\mathrm{R}_{0i} = 9780\left[J\,(\lambda)\kappa^2 n^{-4} Q_i\right]1/6 \quad \text{Eq. 11}$$

$$Q_{Di} = \langle Q_D \rangle \cdot \tau_i / \langle \tau \rangle \quad \text{Eq. 12}$$

$$\langle \tau \rangle = \frac{\sum_{i=1}^{3} A_i \tau_i}{\sum_{i=1}^{3} A_i} \quad \text{Eq. 13}$$

$$\langle Q_D \rangle = Q_S \cdot \left(\frac{F_D(\lambda)}{A_D(\lambda)}\right) \Big/ \left(\frac{F_S(\lambda)}{A_S(\lambda)}\right) \quad \text{Eq. 14}$$

Together, the donor fluorescence (A_i, τ_i) and distance terms (R_j, σ_j) in our analysis were shared globally between all waveforms containing FRET-labeled samples. R_j and σ_j were allowed to vary between 0.5 nm and 15.0 nm. The average Alexa-488/CY3 R_0, (6.7 nm in this study) was determined according to Eq. 11-14. The distance-dependent terms R_j (Eq.9) and σ_j (Eq. 10) define unique structural states of the LCD. The mole fraction terms X_j were allowed to vary independently in each waveform. Thus, changes in X_j reflect changes in the relative populations of the structural states (*j*) as the biochemical state is varied under equilibrium, steady-state, or transient conditions.

We determined the number of donor lifetimes (*i*) and structural states (*j*) that are present in each sample by fitting a set of models with the number of donor lifetime states, *i* increasing from 1 to 4, and the number of structural states, *j*, increasing from 1 to 4. For each model we test a distribution of energy transfer rates, with σ_j allowed to vary, as well as discrete energy transfer rates where $\sigma \rightarrow 0$. The final model ($i_{max} = 2$, $j_{max} = 2$, $\sigma > 0$) was determined by evaluating the dependence of the minimized χ^2 on the number of free parameters in the global model and by the resolution of the χ^2 error surface support plane with a confidence intervals of 67%.

TR-F anisotropy: We analyzed time-resolved fluorescence anisotropy as described in our previous work (7-9) according to Eq. 15-18. The fluorescence lifetime and anisotropy terms are fit globally to the time-resolved fluorescence waveforms acquired with the emission polarizer set at 0°, 90°, and 54.7°. We varied the number of fluorescence lifetimes, τ_i, (Eq. 15-17) and rotational correlation times, τ_{Ri}, (Eq. 18) applied to each biochemical condition.

$$F(54.7°,\ t) = \sum_{i=1}^{3} A_i\ exp(-t/\tau_i) \quad \text{Eq. 15}$$

$$F\ (0°, t) = F(54.7°,\ t) \cdot [1 + 2r(t)]/3 \quad \text{Eq. 16}$$

$$F(90°, t) = F(54.7°,\ t) \cdot [1 - 2r(t)]/3 \quad \text{Eq. 17}$$

$$r(t) = r_\infty + r_i\ exp(-t/\tau_{Ri}) \quad \text{Eq. 18}$$

As described previously, the Alexa-488 donor is best described by a 2-exponential fluorescence decay (i = 2). A single-exponential anisotropy function was sufficient to describe the diffusion of each lifetime. We assumed that each of the Alexa-488 lifetimes experience the same global motion and thus are described by the same anisotropy function. Fitting to independent anisotropy functions did not reveal notable differences in anisotropy between the two lifetime states. The total anisotropy, r_o, was calculated according to Eq. 19.

$$r_0 = \frac{\int_{-\infty}^{\infty} F(54.7°,\ t) \cdot r(t)dt}{\int_{-\infty}^{\infty} F(54.7°,\ t)dt} \quad \text{Eq. 19}$$

$$\langle d_P^x \rangle = \sqrt{r_{0P}/r_f} \quad \text{Eq. 20}$$

$$\langle \kappa^2 \rangle_{min} = \left(\frac{2}{3}\right) \cdot \left(1 - \frac{\langle d_D^x \rangle + \langle d_A^x \rangle}{2}\right) \quad \text{Eq. 21}$$

$$\langle \kappa^2 \rangle_{max} = \left(\frac{2}{3}\right) \cdot \left(1 + \langle d_D^x \rangle + \langle d_A^x \rangle + 3\langle d_D^x \rangle \langle d_A^x \rangle\right) \quad \text{Eq. 22}$$

$$R_{min,max} = [(3/2) \cdot \langle \kappa 2 \rangle_{min,max}]^{1/6} \cdot R(\kappa 2 = 2/3) \quad \text{Eq. 23}$$

We used the total anisotropy to calculate the probe depolarization factors,d_p^x, (Eq.20), with the anisotropy of a rigid assembly of probes, r_f,.of 0.4. The maximum and minimum values of the orientation sensitive term κ^2 were calculated according to Eq. 21 and Eq. 22 and the resulting maximum and minimum range for the average R_0 according to Eq. 23.

Convolution integral and optimization: Nonlinear optimization was performed in software described in previous papers (7-9) and in Matlab using the fmincon optimizer. The TRF models, described above were convolved with the measured instrument response function using a numerical integration routine obtained from the David D. Thomas Laboratory at the University of Minnesota or in Matlab using the "filter" function.

Error support plane analysis. We determined the upper and lower confidence intervals for fit parameters using strategies adapted from Beecham (10, 11) and Johnson (11). (1) Optimization was performed on global data sets containing donor and donor + acceptor labeled samples acquired over a range of biochemical conditions to determine the best-fit parameter values according to the Eq. 1-23. (2) The dependence of the fit χ^2 on variations in each parameter was determined and the upper and lower 67% confidence intervals estimated as the range of values for each parameter that sustains less than a 67% increase in the minimized χ^2.

Transient kinetics of phosphate release. We detected dissociation of inorganic phosphate from myosin using phosphate-binding protein (PBP) labeled with MDCC(12). Reagents for the expression or PBP were provided by Dr. Howard White (13). The purification and characterization of phosphate-binding protein (PBP) was performed as described in our previous work (7). For experiments measuring the kinetics of actin-activated phosphate dissociation, MDCC-PBP (10 μM) was included in all syringes, along with phosphate mop (5, 12, 13), which is added to remove contaminating free phosphate present in buffers, samples, and the stopped-flow instrument.

Cy3-ATP: We purchased the Cy3-ATP and Cy3-ADP used in this study from *Jena Bioscience*. These reagents are > 95% pure by the manufacturer's specifications.

The absorbance, excitation, and emission spectra of the Alexa-488 donor and Cy3-ATP nucleotides, do not change during ATPase cycling. We measured the absorbance, excitation, and emission spectra of the Alexa-488 donor labeled myosin and the Cy3 nucleotides used in this study over a range of biochemical conditions. The photophysical properties of the Alexa donor did not change with the biochemical condition of the sample (Fig. S3). The Cy3 nucleotides used in this study undergo a well-documented increase in fluorescence when they bind to the nucleotide binding pocket of myosin (14-16). We verified that this change does not reflect a change in the absorbance extinction coefficient of the Cy3 probe (Fig. S3). Furthermore, the fluorescence enhancement detected upon binding is solely associated with a change in quantum yield (Fig. S3) as the normalized excitation spectra (Fig. S3) are identical for Cy3-nucleotides in solution or Cy3-ADP or Cy3-ADP.Vanadate bound by saturating excess of HMM (Fig. S3). These controls indicate that the spectral overlap between the donor Alexa probe and the bound Cy3 nucleotides does not change when the nucleotides bind, nor is the spectral overlap dependent on the ATP hydrolysis state, thus the average R_0, which we determined to be 6.7 nm, does not change during ATPase cycling.

Cy3 fluorescence does not contaminate the measured Alexa-488 signal. Any Cy3 emission that passes through the 520 nm band-pass filter (*Semrock*) used to isolate the Alexa-488 emission in our experiments would affect the interpretation of TR-FRET and the structural kinetics modeling. Thus, we verified that even in the presence of 10 molar excess Cy3-ATP or Cy3-ADP, the Cy3-emission that passes through the 520 nm band pass filter as the result of direct excitation by the 473 nm laser or by excitation via FRET, is not significant (Fig. S3).

Time-resolved fluorescence anisotropy and κ^2. We determined that the time-resolved anisotropy of the Alexa donor is not sensitive to the biochemical state of the myosin and the anisotropy of the Cy3-ATP bound to myosin is the same as Cy3-ADP and Cy3-ATP (Table S4) and thus does not change during the weak-to-strong actin-binding transition. Furthermore, the Alexa donor, which exhibits a nanosecond fluorescence lifetime, rotates with a correlation time on the nanosecond time-scale (Table S4), and the maximum and minimum uncertainties in R_0 resulting from the uncertainty of κ^2, (Eq. 19-23) were 6.5 and 8.0 respectively. This indicates that the measured FRET is primarily dependent on the distance between the probes and not a change in probe orientation. Thus TR-FRET between the labeled RLC and Cy3-nucleotides, detects the rotation of the LCD.

Kinetics Simulations: We used KinTek Explorer (11, 17, 18) to model the structural kinetics of LCD rotation and phosphate release. Mole fractions of the M** and M* states after mixing with varied [Cy3-ATP] or 2 μM Cy3-ATP and then varied [Actin] as described for , and released [P_i] were modeled by simultaneously fitting either kinetic mechanisms 1 (Eq. 24) , 2 (Eq. 25), or 3 (Eq. 26) in KinTek Explorer. We evaluated the fit χ^2 (Fig. S7) to determine which mechanism best describes the observed data. The χ^2 from mechanism 1 (Fig. S7) was 8 times greater than mechanism 2 despite having the same degrees of freedom. Mechanism 3, which allows for both the phosphate first and the power stroke first pathways, did not improve the χ^2 despite increased model complexity. This analysis demonstrates that the phosphate first mechanism does not describe the data.

$$M^0 + ATP \overset{K_1}{\leftrightarrow} M^*T \overset{K_2}{\leftrightarrow} M^{**}DP + A \overset{K_3}{\leftrightarrow} AM^{**}DP \overset{k_{+4}}{\rightarrow} AM^{**}D + P \overset{K_5}{\leftrightarrow} AM^*D \overset{K_6}{\leftrightarrow} AM^0 + D \quad \text{Eq. 24}$$

$$M^0 + ATP \overset{K_1}{\leftrightarrow} M^*T \overset{K_2}{\leftrightarrow} M^{**}DP + A \overset{K_3}{\leftrightarrow} AM^{**}DP \overset{K_4}{\leftrightarrow} AM^*DP \overset{k_{+5}}{\rightarrow} AM^*D + P \overset{K_6}{\leftrightarrow} AM^0 + D \quad \text{Eq. 25}$$

$$\begin{array}{l} M^0 + ATP \overset{K_1}{\leftrightarrow} M^*T \overset{K_2}{\leftrightarrow} M^{**}DP + A \overset{K_3}{\leftrightarrow} AM^{**}DP \overset{k_{+4}}{\rightarrow} AM^{**}D + P \\ \qquad\qquad\qquad\qquad\qquad\qquad\qquad\qquad\qquad\qquad K_5 \updownarrow \qquad\qquad K_6 \updownarrow \\ \qquad\qquad\qquad\qquad\qquad\qquad\qquad\qquad\qquad\quad AM^*DP \overset{k_{+7}}{\rightarrow} AM^*D + P \overset{K_8}{\leftrightarrow} AM^0 + D \end{array} \quad \text{Eq. 26}$$

Table S1. Predicted TR-FRET distance distribution center determined by measuring the distance between the α-carbon of residues homologous to chicken gizzard smooth muscle myosin RLC C108, and the 2' oxygen of bound or modeled ADP ribose in the pre-power stroke and rigor like crystal structures. For 1Br1, the scallop RLC was modeled onto the smooth muscle myosin heavy-chain. Estimate uncertainties +/- 1.0 nm assuming 0.5 nm probe linkers.

State	Distance (PDB)	Lower Estimate	Upper Estimate
Pre-Power	5.5 (1Br1)	4.5	6.5
Rigor-Like	6.8 (2MYS)	5.8	7.8
""	7.5(1DFL)	6.5	8.5
""	8.5(1DFK)	7.5	9.5
""	9.0(1KQM)	8	10
""	8.4(1KK7)	7.4	9.4

Table S2. Steady-state and transient kinetics measured in this paper. Steady-state activities as determined in Fig. S1, observed transient structural kinetics from Fig. 3, and modeled structural kinetics from kinetic modeling in Fig. S7.

Steady-state ATPase			
	Unlabeled	**Labeled**	
$V_{max(actin)}$	12.9 ± 0.5 s^{-1}	13.4 ± 0.6 s^{-1}	
$K_{m(actin)}$	22.0 ± 2.0 μM	22.2 ± 2.3 μM	
Basal	0.01 ± 0.005 s^{-1}	0.01 ± 0.005 s^{-1}	
Transient Biochemical and Structural Kinetics			
Transition	**forward**	**reverse**	$K_{(app)}$
ATP Binding	4.0 μM^{-1} s^{-1}	< 0.1 s^{-1}	$K_{(app)}$ < 25 nM
P_i Release acto-skS1	35 s^{-1}	—	—
P_i Release acto-skHMM	35 s^{-1}	—	—
P_i Release acto-skHMM(smRLC)	38 s^{-1}	—	—
Weak Actin Binding	7.0 μM^{-1} s^{-1}		> 100 μM
Actin-induced LCD rotation pre-dead time	> 1000 s^{-1}		0.6
Actin-induced LCD rotation (phase-1)	> 500 s^{-1}		1.1
Actin-induced LCD rotation (phase-2)	35 s^{-1}		19
Actin-induced LCD rotation (phase-3)	3 s^{-1}		—
Modeled Structural Kinetics			
Transition	**forward**	**reverse**	K_{eq}
ATP Binding	3.9 ± 0.03 μM^{-1} s^{-1}	< 0.1	< 25 nM
Recovery/Hydrolysis	294 ± 36.8 s^{-1}	109 ± 14.2 s^{-1}	2.7
Weak Actin Binding	15.8 ± 5.5 μM^{-1} s^{-1}	1200 ± 400 s^{-1}	135 μM
LCD Rotation	689± 33 s^{-1}	109± 3.9 s^{-1}	6.3
Pi Release	17.9± 0.14 s^{-1}	—	—
ADP Release	>1000 s^{-1}	—	—

Table S3. Time-Resolved fluorescence lifetime parameters for donor and donor + acceptor labeled HMM at 25°C. Upper and lower 67% confidence bounds determined from χ^2 support plane error analysis (described in SI Methods).

Parameter	Best-Fit	Lower Bound	Upper Bound
Donor only			
Amplitude τ_1	0.81	0.80	0.81
$\tau_{1\,(ns)}$	3.86	3.85	3.87
Amplitude τ_2	0.19	0.20	0.19
$\tau_{2\,(ns)}$	1.49	1.45	1.54
Distance distributions			
R1 (nm)	5.7 ±0.007	5.52	5.96
FWHM 1 (nm)	2.7 ±0.05	2.04	2.92
R2 (nm)	10.3 ±0.09	10.06	10.63
FWHM 2 (nm)	6.6 ±0.21	5.06	8.22

Table S4. Time-Resolved Anisotropies and Correlation Times for Alexa-488-Labeled HMM of Cy3-nucleotides bound to excess non-labeled HMM at 25°C.

	Biochemical State			
Alexa-488	**Apo**	**ATP/ADP.P_i**	**ADP**	**Actin**
Initial Anisotropy	0.31 ± 0.01	0.31 ±0.01	0.31 ±0.01	0.29 ±0.01
Correlation Time (ns)	2.02 ±0.23	1.66 ± 0.36	2.12 ± 0.22	1.59 ± 0.23
Final Anisotropy	0.16 ± 0.005	0.16 ± 0.006	0.16 ± 0.004	0.15 ± 0.004
r_o	0.29	0.30	0.29	0.27
Cy3-ATP	**Apo**	**ATP/ADP.P_i**	**ADP**	**Actin**
r_o	—	0.33 ±0.01	0.33 ±0.01	—
Cy3-ADP	**Apo**	**ATP/ADP.P_i**	**ADP**	**Actin**
r_o	—	0.33 ± 0.01	0.33 ± 0.01	—
κ^2_{min}	0.57	0.57	0.57	0.58
κ^2_{max}	2.02	2.04	2.02	1.98
$R_{0\ min}$	6.54	6.54	6.54	6.54
$R_{0\ min}$	8.03	8.03	8.03	8.03

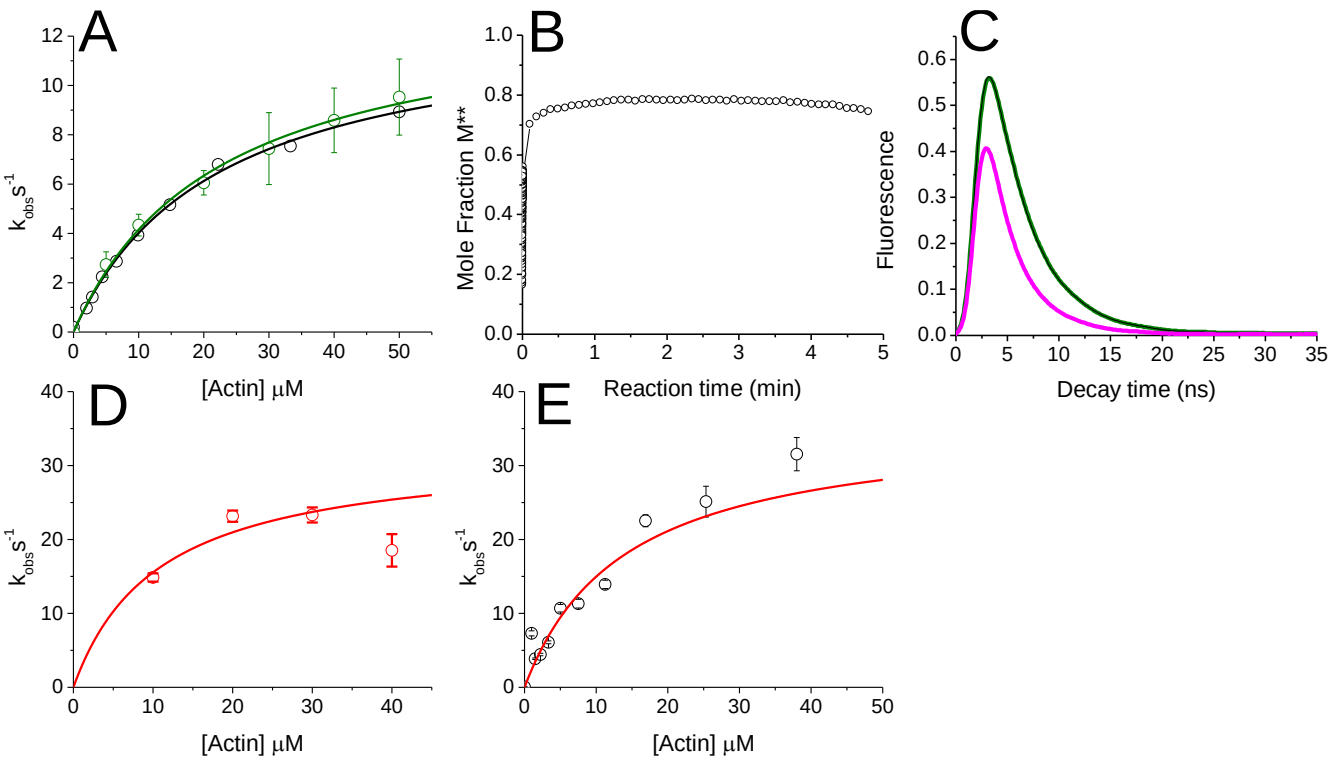

Fig. S1. Steady-state actin-activated ATPase, nucleotide binding and actin-activated turnover. (A) Steady-state ATPase activity of Alexa-488 labeled HMM (green, best-fit function, $ATPase = 13.4\,[Actin]/(22 + [Actin])$ and non-labeled HMM (black, $ATPase = 12.9\,[Actin]/(22 + [Actin])$). (B) Steady-state stability of the Alexa-HMM:Cy3ATP complex under conditions used in this study. The Cy3-ATP dependent M** state is stable for more than 2 minutes after mixing 0.1 μM HMM with 2 μM (10 molar excess) Cy3-ATP. (C) Representative TR-FRET waveforms under steady-state ATPase cycling as in B, in the presence (green) or absence (magenta) of actin or in the absence of Cy3-ATP (black). (D and F) Actin-activated single-turnover with Cy3-ATP (D, best-fit function, $k_{obs} = 32.0\,[Actin]/(10 + [Actin])$) or mant-ATP (E, best-fit function, $k_{obs} = 35.0\,[Actin]/(14 + [Actin])$). N = 3, errors calculated as SEM of replicate experiments.

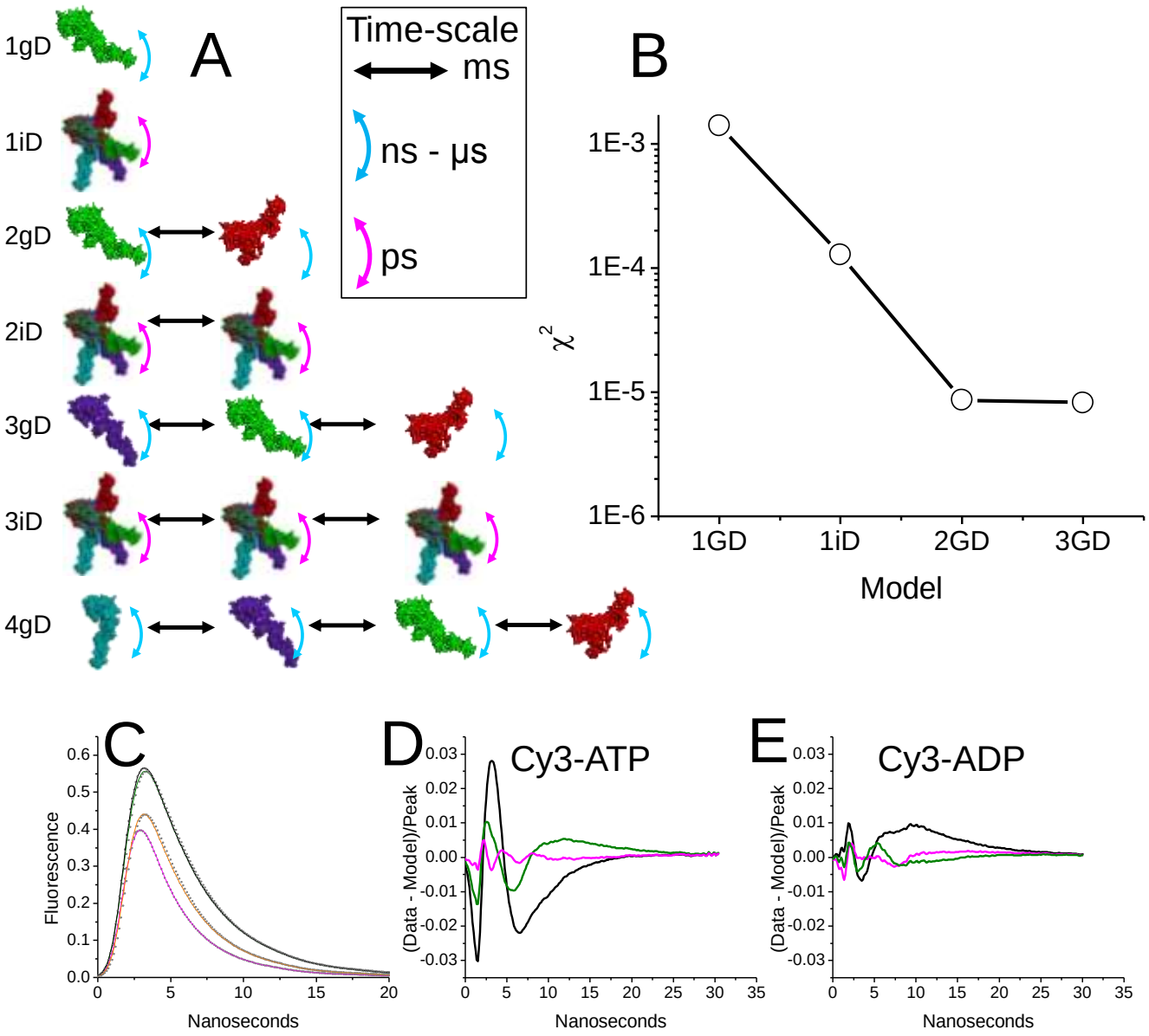

Fig. S2. Structure-based TR-FRET model validation. (A) Models tested in this study are noted by the number of distance distributions (1, 2, 3, 4) the dependence of the center and width of the distribution on the biochemical conditions (g, global center and width shared over all biochemical states, i, independent center and width allowed to vary over all biochemical states) . Thus 2gD (the best-fit model in this study) is a model with 2 global distance distributions with the center and width of the distributions common to all biochemical states. In the 2gD model, changes in TR-FRET reflect changes in the mole fractions for each distance distribution as described in Eq. 4. In the independent models (1iD, 2iD, 3iD) the continuous variation of distance distributions indicates conformational exchange on the picosecond to nanosecond timescale (magenta arrow indicated in panel A inset box), while in the global models (1gD, 2gD, 3gD, 4gD), the distance distribution center and width do not vary and exhibit µs motion (blue arrow indicated in panel a inset box). Linear black arrows indicate structural transitions occurring on the millisecond time scale. (B) χ^2 for models tested in this study. Increasing the model complexity beyond 2gD does not improve the fit. (C). Typical waveforms obtained under equilibrium or steady-state biochemical conditions. HMM Alexa-488 donor only (black), HMM Alexa-488 + Cy3-ATP mixed with Actin + 1 mM ATP (green, indistinguishable from donor), HMM Alexa-488 + saturating Cy3-ADP (orange), HMM Alexa-488 + saturating Cy3-ATP (magenta). Data shown as open symbols, 2GD best-fit model shown as lines. (D and E) Residuals (data –model): HMM Alexa-488 + saturating Cy3-ATP (D) or Cy3-ADP (E) for 1gD (black), 1iD (green), or 2gD (magenta) models.

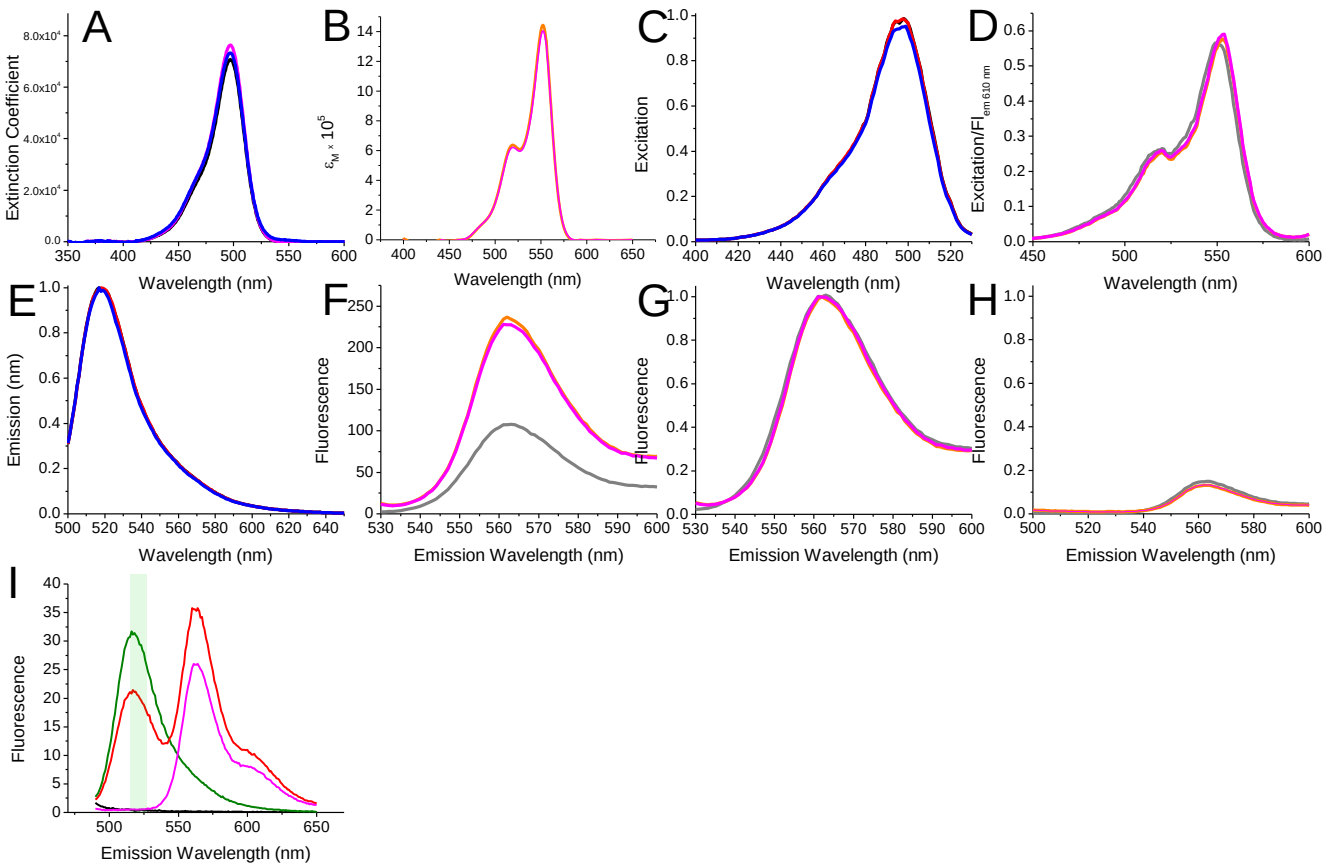

Fig. S3. Absorbance, excitation, and emission spectra of fluorescent probes used in this study. (A) Absorbance molar extinction coefficient of Alexa-488 labeled HMM (black) or in the presence of excess MgATP (magenta), or actin (blue) showing that the absorbance spectra of the donor does not change with nucleotide of actin binding. Differences in peak absorbance are within the error of sample preparation (5%), and background subtraction. (B) Absorbance molar extinction coefficient of Cy3-ADP (orange) or Cy3-ADP.Vanadate (magenta) bound to non-labeled HMM showing that the absorbance of the acceptor does not change with binding to myosin. (C) Excitation spectra of samples in panel a, monitoring emission at 550 nm showing that the excitation spectra does not change with biochemical state. (D) Excitation spectra of Cy3-ADP in solution (grey) or bound (orange) to HMM or Cy3-ADP.Vanadata bound (magenta) to HMM showing that the excitation spectra of the acceptor does not change with biochemical state. (E). Emission spectra of Alexa-488 labeled HMM samples from panel a showing that the donor fluorescence emission does not change with biochemical state. (F) Emission spectra of Cy3-ADP or Cy3-ADP.Vanadate excited at 520 nm in the absence (grey) or presence (orange and magenta respectively) of HMM showing that the acceptor undergoes an increase in quantum yield with binding, but that the emission does not change with the ATP hydrolysis state. (G) Data in (F) normalized to emission peak showing that the shape of the acceptor emission spectra do not change. (H) Emission spectra as in (G) upon excitation at 473 nm to check for direct excitation of the Cy3 by the 473 nm laser used in this study. (I) Emission spectra of 0.2 μM donor-labeled HMM (green), 0.2 μM donor-labeled HMM with 2 μM Cy3-ATP or Cy3-ATP alone (red) upon excitation at 473 mM. The fluorescence of the bound acceptor does not contribute to the 520 nm detection window (green box) used to monitor donor emission.

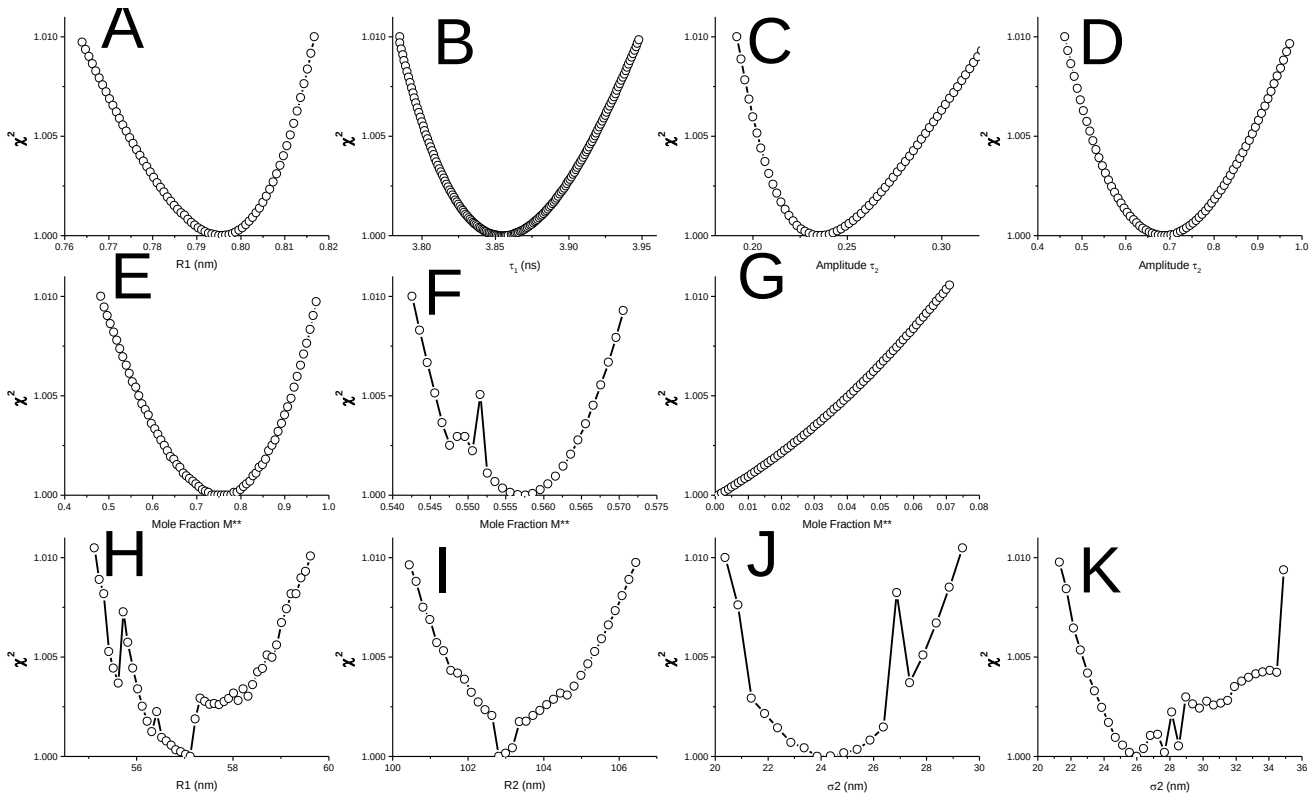

Fig. S4. Representative confidence interval (67%) support plane for best-fit parameters determined in this study showing dependence of fit χ^2 on variation in fit parameters within the 67% confidence interval. Upper and Lower bounds in Table S3 and Table S4 determined from the width of the error surfaces. (A) Donor time-resolved fluorescence τ_1 pre-exponential factor, (B) τ_1 lifetime, (C) τ_2 pre-exponential factor, or (D) τ_1 lifetime. The M** mole fraction (E) under steady-state ATPase cycling conditions, (F) at the start of the actin-induced power stroke or (G) after completing the power stroke. (H) M** distance distribution center, (I) M* distance distribution center, (J) M** FWHM, (K) M* FWHM. Error plane computed as described in SI.

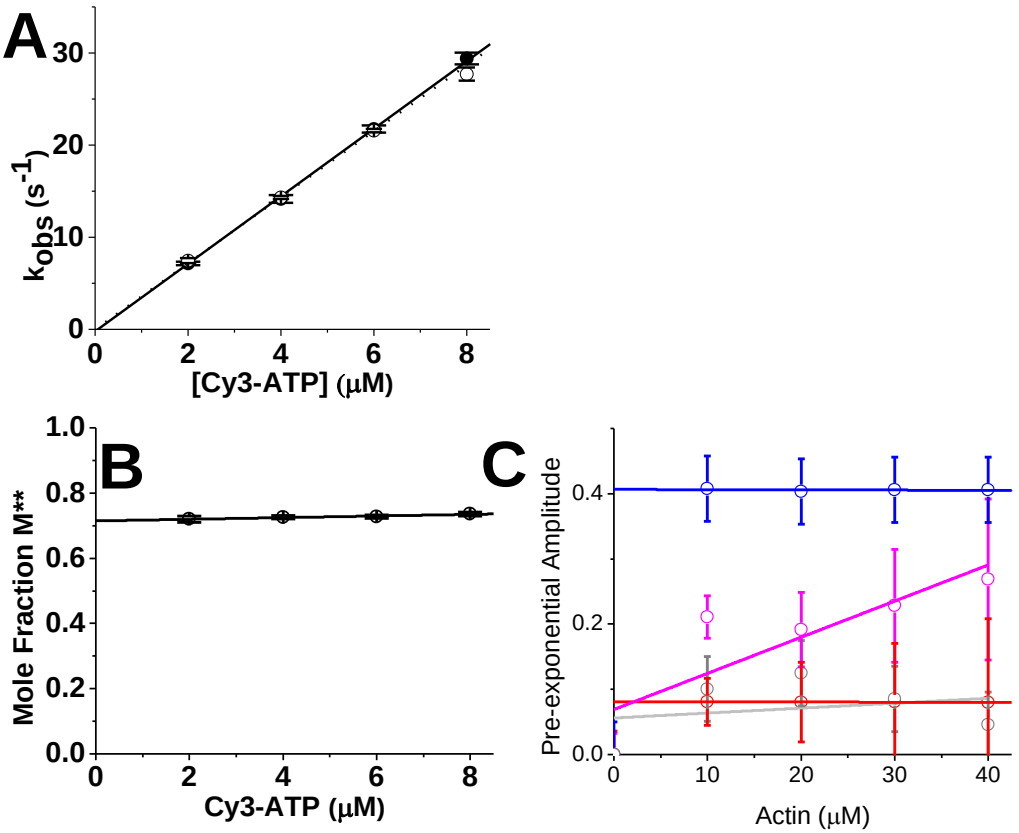

Fig. S5. Supplemental observed kinetics for transient changes in FRET measured in this study. (A) Observed rate constants for Cy3-ATP binding, determined as described in Fig. 2, total fluorescence transients (open symbols, dotted lines), mole fraction M* transients (solid symbols, solid lines). (B) Pre-exponential amplitudes for M* mole fraction transients during Cy3-ATP binding described in Fig. 2. (C) Pre-exponential amplitudes for 3 exponential fits of M* transients described in Fig. 2 during the actin induced power stroke, pre-dead time rapid equilibrium (magenta), phase 1 (red), phase 2 (blue), 3.4 $^{s-1}$ slow phase (grey).

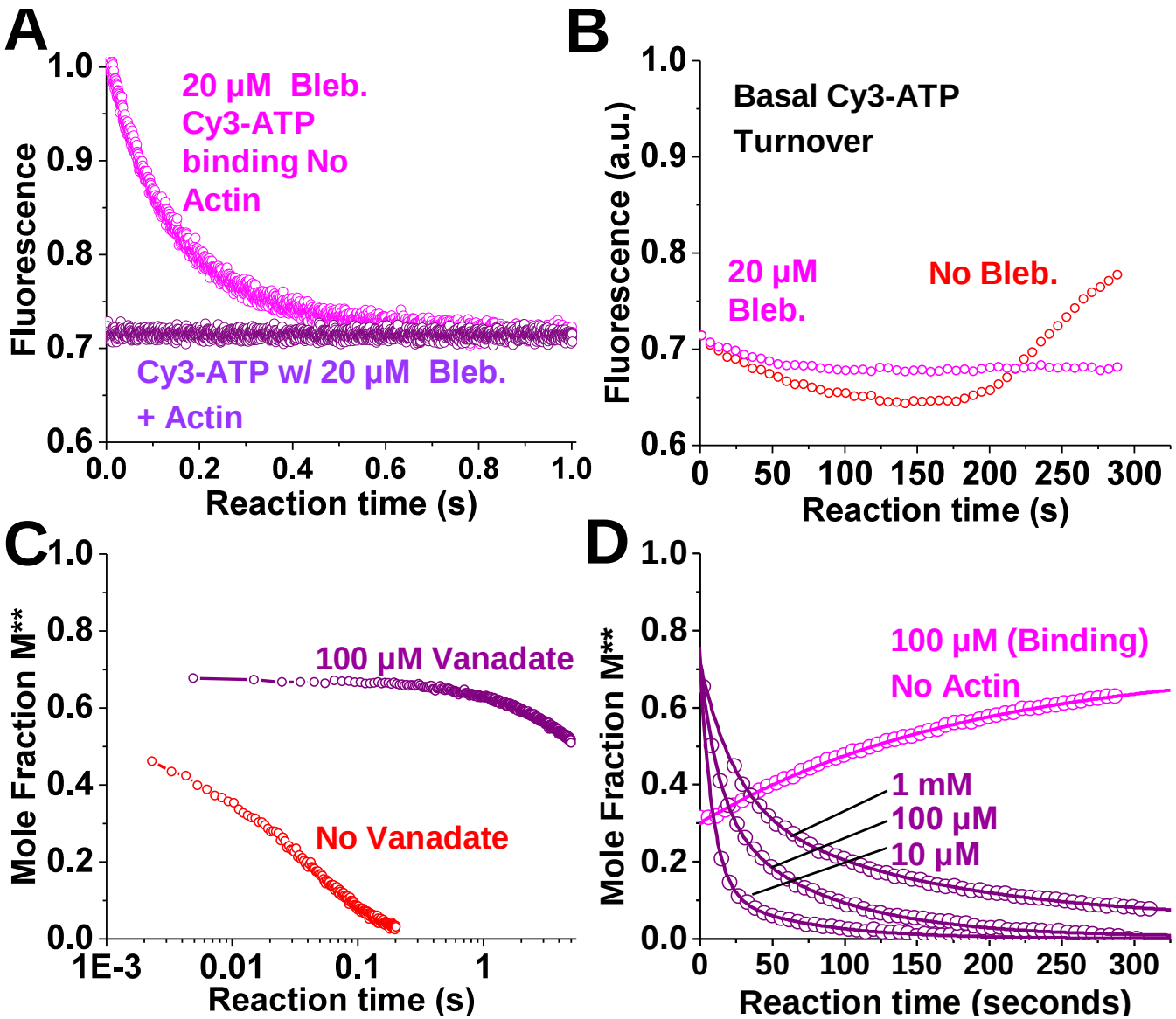

Fig. S6. Blebbistatin and vanadate inhibit LCD rotation. (A) Standardized total fluorescence after mixing 0.2 μM donor-labeled HMM and 20 μM blebbistatin with 2 μM Cy3-ATP (magenta) and then with 40 μM Actin (purple). (B) Standardized total fluorescence after mixing 0.2 μM donor-labeled HMM, in the presence (magenta) or absence (red) of 20 μM blebbistatin, with 2 μM Cy3-ATP. (C) M** mole fraction obtained from $(TR)^2$FRET after mixing 0.2 μM donor-labeled HMM with 2 μM Cy3-ATP (red) or 2 μM Cy3-ADP and 100 μM Vanadate with actin (40 μM post-mix, purple). (D) M** mole fraction after mixing 0.2 μM donor-labeled HMM and 2 μM Cy3-ADP with 100 μM vanadate (magenta) or with 40 μM actin and varied [vanadate] (purple). Solutions contained 2 mM $MgCl_2$, 10 mM Tris (pH 7.5), 25 C.

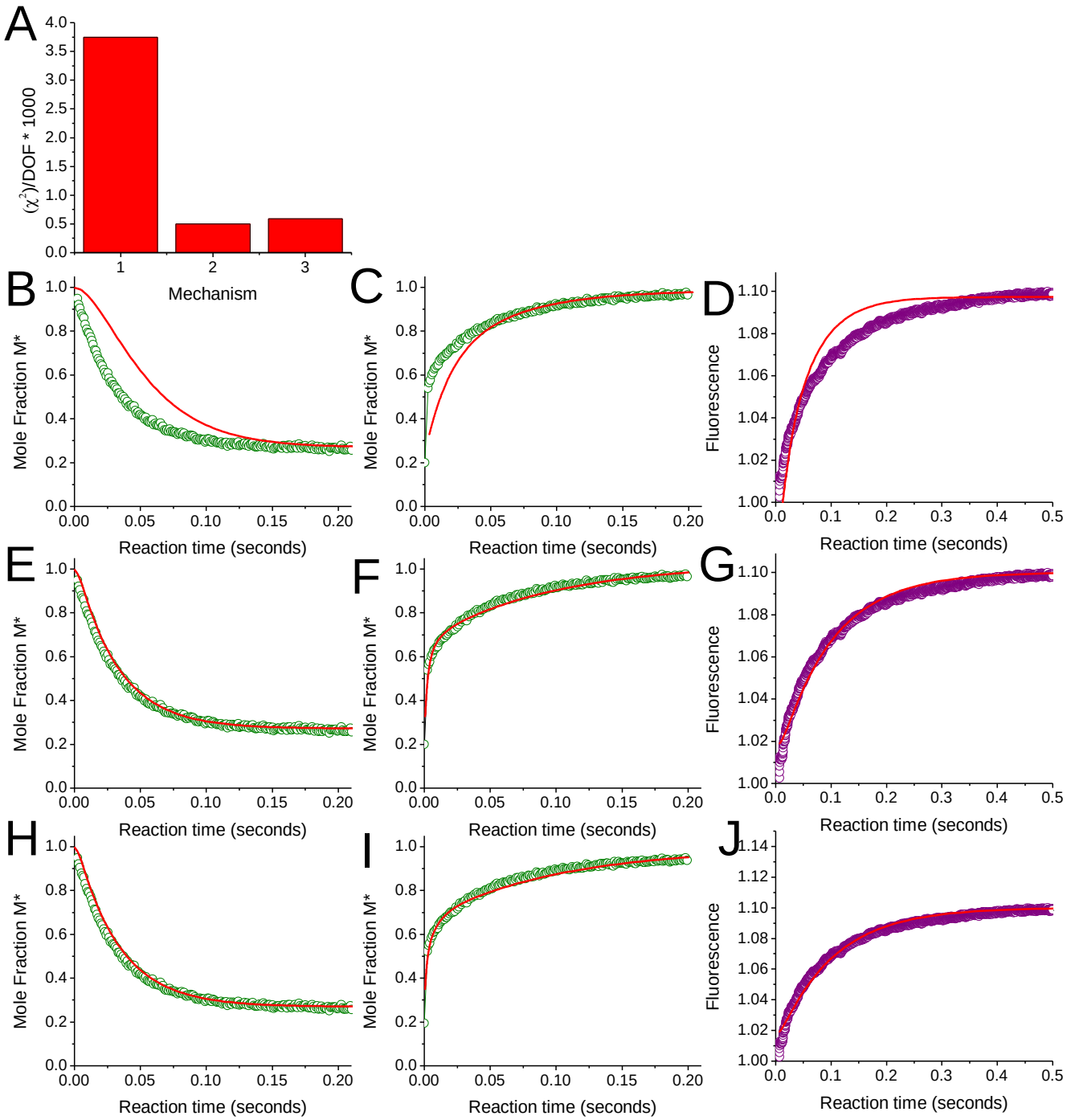

Fig. S7. Global structural kinetics modeling of the power stroke and phosphate release. (A) χ^2 for global kinetic fitting of mechanism 1 (phosphate-first), 2 (power stroke first), or 3 (branched) to mole fraction and phosphate release data using KinTek Explorer (SI). (B-D) Comparison of data (symbols) and fit (red line) for mechanism-1 fitting, mechanism-2 (E-G), or mechanism-3 (H-J). (B, E, H) Mole fraction M* during ATP binding driven recovery/hydrolysis phase in the absence of actin (data obtained as described in a, 8 μM Cy3-ATP shown). (C, F, I) Mole fraction M* during actin-induced single ATP turnover (data obtained as described in Fig. 2, 40 μM actin shown). (D, G, J) Phosphate release detected by fluorescence of phosphate binding protein during actin-induced single ATP turnover (data obtained as described in Fig. 3, 40 μM actin shown).

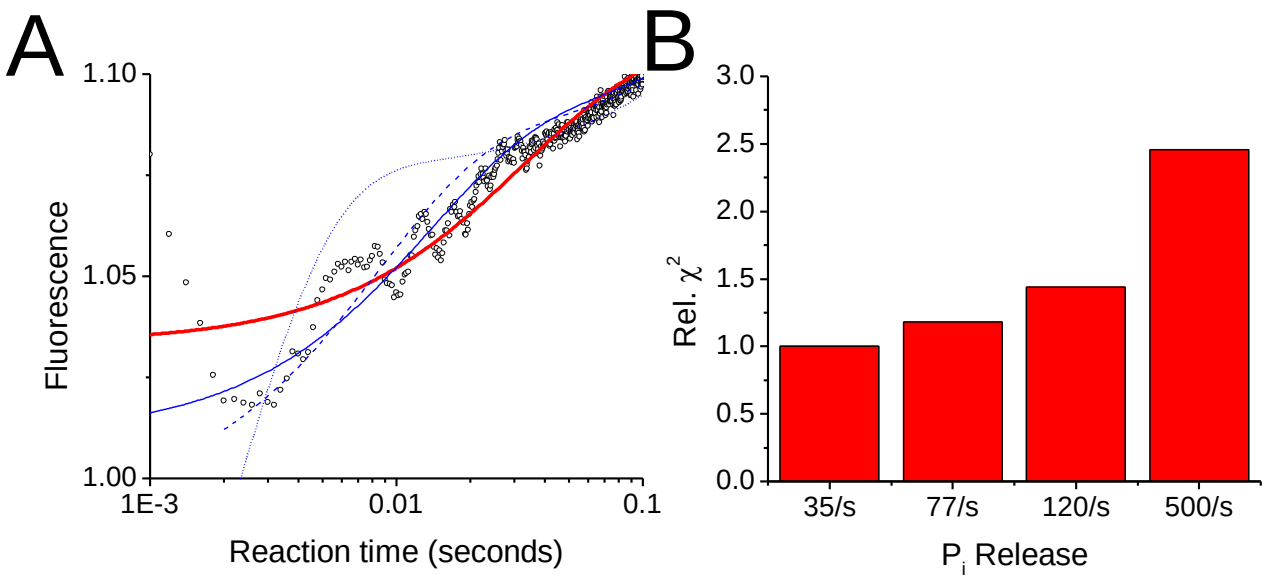

Fig. S8. Sensitivity analysis of phosphate release observed rate constant. (A) Phosphate release detected with mdcc-PBP after mixing with 40 μM [actin] as performed in Fig. 3. Data fit with $I(t) = y0 + A1\ e^{-k1\ t} + A2\ e^{-k2\ t}$ fixing k1 at 35 s^{-1} (red line), 77 s^{-1} (solid blue line), 120 s^{-1} (dashed blue line), 500 s^{-1} (dotted blue line). (B) Reduced χ^2 normalized to best fit reduced χ^2.

Supplemental Appendix References

1. Margossian SS & Lowey S (1982) Preparation of myosin and its subfragments from rabbit skeletal muscle. (Translated from eng) *Methods Enzymol* 85 Pt B:55-71 (in eng).
2. Kast D, Espinoza-Fonseca LM, Yi C, & Thomas DD (2010) Phosphorylation-induced structural changes in smooth muscle myosin regulatory light chain. (Translated from eng) *Proc Natl Acad Sci U S A* 107(18):8207-8212 (in eng).
3. Prochniewicz E, Walseth TF, & Thomas DD (2004) Structural dynamics of actin during active interaction with myosin: different effects of weakly and strongly bound myosin heads. (Translated from eng) *Biochemistry* 43(33):10642-10652 (in eng).
4. Hopkins SC, *et al.* (2002) Orientation changes of the myosin light chain domain during filament sliding in active and rigor muscle. (Translated from eng) *J Mol Biol* 318(5):1275-1291 (in eng).
5. De La Cruz EM & Ostap EM (2009) Kinetic and equilibrium analysis of the myosin ATPase. (Translated from eng) *Methods Enzymol* 455:157-192 (in eng).
6. Brissette P, Ballou DP, & Massey V (1989) Determination of the dead time of a stopped-flow fluorometer. (Translated from eng) *Anal Biochem* 181(2):234-238 (in eng).
7. Muretta JM, Petersen KJ, & Thomas DD (2013) Direct real-time detection of the actin-activated power stroke within the myosin catalytic domain. (Translated from eng) *Proc Natl Acad Sci U S A* 110(18):7211-7216 (in eng).
8. Nesmelov YE, *et al.* (2011) Structural kinetics of myosin by transient time-resolved FRET. (Translated from eng) *Proc Natl Acad Sci U S A* 108(5):1891-1896 (in eng).
9. Muretta JM, *et al.* (2010) High-performance time-resolved fluorescence by direct waveform recording. (Translated from eng) *Rev Sci Instrum* 81(10):103101 (in eng).
10. Beechem JM (1992) Global analysis of biochemical and biophysical data. (Translated from eng) *Methods Enzymol* 210:37-54 (in eng).
11. Johnson KA (2009) Fitting enzyme kinetic data with KinTek Global Kinetic Explorer. (Translated from eng) *Methods Enzymol* 467:601-626 (in eng).
12. Brune M, Hunter JL, Corrie JE, & Webb MR (1994) Direct, real-time measurement of rapid inorganic phosphate release using a novel fluorescent probe and its application to actomyosin subfragment 1 ATPase. (Translated from eng) *Biochemistry* 33(27):8262-8271 (in eng).
13. White HD, Belknap B, & Webb MR (1997) Kinetics of nucleoside triphosphate cleavage and phosphate release steps by associated rabbit skeletal actomyosin, measured using a novel fluorescent probe for phosphate. (Translated from eng) *Biochemistry* 36(39):11828-11836 (in eng).
14. Kuhlman PA & Bagshaw CR (1998) ATPase kinetics of the Dictyostelium discoideum myosin II motor domain. (Translated from eng) *J Muscle Res Cell Motil* 19(5):491-504 (in eng).
15. Conibear PB, Kuhlman PA, & Bagshaw CR (1998) Measurement of ATPase activities of myosin at the level of tracks and single molecules. (Translated from eng) *Adv Exp Med Biol* 453:15-26; discussion 26-17 (in eng).
16. Chaen S, Shirakawa I, Bagshaw CR, & Sugi H (1998) Measurement of ATP turnover during shortening and lengthening of rabbit psoas myofibrils using a fluorescent ATP analog. (Translated from eng) *Adv Exp Med Biol* 453:569-576 (in eng).
17. Johnson KA, Simpson ZB, & Blom T (2009) Global kinetic explorer: a new computer program for dynamic simulation and fitting of kinetic data. (Translated from eng) *Anal Biochem* 387(1):20-29 (in eng).
18. Johnson KA, Simpson ZB, & Blom T (2009) FitSpace explorer: an algorithm to evaluate multidimensional parameter space in fitting kinetic data. (Translated from eng) *Anal Biochem* 387(1):30-41 (in eng).